International Forum on Aeroelasticity and Structural Dynamics
IFASD 2024
17-21 June 2024, The Hague, The Netherlands

NONLINEAR GUST EFFECTS ON FLEXIBLE AIRCRAFT WITH FLARED HINGED WINGS

Kelvin Chi-Wing Cheng[1], Alvaro Cea Esteban[1], Rafael Palacios[1], Andrea Castrichini[2], Thomas Wilson[2]

[1]Department of Aeronautics, Imperial College London
SW7 2AZ, United Kingdom
kelvin.cheng@imperial.ac.uk
alvaro.cea-esteban15@imperial.ac.uk
r.palacios@imperial.ac.uk

[2]Airbus Operations, Ltd.
BS99 7AR, United Kingdom
andrea.a.castrichini@airbus.com
thomas.wilson@airbus.com

Keywords: Flight dynamics, aeroelasticity, HALE aircraft, flared hinged wings, folding wing tips, gust load alleviation

Abstract: This paper presents a study on the modelling and coupled dynamic analysis of a flexible aircraft with flared hinged wings. A geometrically-exact composite beam model in a non-stationary reference frame, complemented with Lagrange multipliers to enforce multibody constraints, is coupled with unsteady vortex lattice aerodynamics to perform time domain simulations. A full-vehicle configuration featuring flared hinged wing tips is introduced, based on a high-altitude long-endurance T-tail aircraft. Aeroelastic trim and equilibrium states are computed for both the original vehicle and the modified aircraft with hinged wing tips, for the analysis of 1g plus gust responses in the vertical and lateral directions. Results shed light on the coupled nonlinear aeroelastics and flight dynamics exhibited by various HALE configurations in gust encounters of various intensities. It is found that the response of the aircraft with flared hinged wings considering geometrical nonlinearities is predominantly bounded by that of the stretched and upturned wing tips cases, with nonlinear trends uncovered and weighed in their contributions to the overall coupled system dynamics of aircraft configured as such.

1 INTRODUCTION

The net zero target by 2050 in aviation calls for disruptive thinking at the systems level. Apart from efficiency gains in operations and fuel choice, one major contribution of carbon remains the manufacturing and design of aircraft [1]. One of the many avenues to achieve cuts in emissions is the development of weight-saving technologies in aircraft design, to which there are many answers. It is shown that with the current architecture of wing design, in the absence of a paradigm shift in technologies deployed, by fine-tuning the global aero-structural design of current wings we can only achieve single digit weight savings in a controlled environment [2]. One of those more mature (on the TRL scale) next-generation technologies from biomimicry is a morphing aerostructure for active load alleviation [3], which despite the complexities in implementation and failure modes remains promising [4]. Another example would be the use of folding wing tips [5, 6], in particular ones that allow for free-flapping motion inflight akin to

that of birds, to exploit the potential gust load alleviation and manoeuvring advantages, while remaining locked: extended at 0° for cruise, and upwards at 90° for taxiing, the latter to comply with gate restrictions. Arguably the most important feature of the hinge is the flare angle - this describes how the hinge axis is oriented with regards to the freestream direction. A hinge axis pointing towards the centerline downstream produces a restoring force by the change of angle of incidence due to rotation of the wing tips when perturbed in either direction from trim, ensuring the mechanism is statically stable.

Much work has been done in both the modelling and experimentation aspects of the problem and computational results have largely established the aeroelastic performance of flared folding wing tips [7–13]. Recent advances have been made in multiple directions, assessing the viability of such a wing tip device, all converging to the eventual goal of realising the concept in a commercial transport aircraft - these include a better understanding of the impact of wing stiffness and release timing [14] on the load-alleviating properties of the mechanism, the stability boundary as a function of an additional trim device on the folding wingtip, model parameters, and types of nonlinearities involved [15], the folding wing tips featuring in a scaled wind tunnel model aircraft with high aspect ratio wings [16], the extrapolation of wind tunnel results to a full-size model via scaling methods [17], the improvements on roll performance by reducing the roll damping and increasing the peak acceleration achieved seen on a scaled model in wind tunnel tests and associated numerical modelling [18], and the assessment of varying degrees of roll maneuverability by control surface location and dynamic pressure in the transonic regime [19].

To profile the transient response of the wing assembly with the hinge mechanism it is essential that we incorporate the nonlinear effects of large displacements and rotations, both in the main, usually flexible wing, as well as the wing tips, which can assume a wide range of configurations depending on dynamical conditions. It is often computationally prohibitive to perform trade studies on the aeroelastic wing assembly with higher-fidelity tools such as 3D CFD coupled with 3D FEM.

Therefore, a framework is being developed on SHARPy [20], an open-source, nonlinear aeroelastic simulation toolbox [1], which couples unsteady aerodynamics (with the unsteady vortex lattice method (UVLM)) with a structural description given by a nonlinear geometrically-exact composite beam model (GEBM)). In this work, we will demonstrate the capabilities of the nonlinear aeroelastic multibody formulation with the aeroelastic simulation of a multibody high altitude long endurance (HALE) aircraft. We aim to shed light on how the static (at trim) and dynamic load alleviation in vertical and lateral gust are affected by gust intensity, and how they compare with the baseline cantilever and upturned wing tip configurations.

2 THEORY AND IMPLEMENTATION

2.1 Nonlinear aeroelastic simulation environment

This section outlines the theory and implementation of the simulation environment for flexible aircraft dynamics, in particular, the parts concerning flexible multibody dynamics.

[1] available at `https://github.com/ImperialCollegeLondon/sharpy`

2.1.1 Definition of reference frames and kinematics

Figure 1 defines the notation, used to describe the kinematics of the flexible wing with hinged wing tips. We begin from the Earth frame E in Figure 1a, from which we define $\mathfrak{p}(t)$ as the time-varying vector to the body-attached frame B used to track the vehicle and define its absolute orientation. In this paper the right-handed B frame is at the root of the wing, with positive x direction towards the right wing, and positive z direction upwards. The rotation matrix from E to B frame $\mathbf{R}_{BE}$ is defined with a choice of parametrisation, in this case the quaternion χ^B, for the generality of the description. In the B frame we define $\boldsymbol{r}_B^G$ as the vector to the material frame at the tip of the main wing, frame G. The rotation matrix from B to G frame $\mathbf{R}_{GB}$ is defined, again with a choice of parametrisation, in this case the Cartesian Rotation Vector (CRV) $\boldsymbol{\psi}_B^G$, for CRVs only uses three DoFs which corresponds to the usual linear rotations for infinitesimal rotations.

On the wing tip itself in Figure 1b, separated by the hinge, we define the body-attached frame H at its root where the rotation matrix from the global frame $\mathbf{R}_{HE}$ is a function of the quaternion χ^H, without loss of generality, and for ease of expressing common quantities in the Earth frame in the later sections. Inertial velocities of body-fixed frames, i.e., B and H, are given in their own FoRs respectively by $\boldsymbol{v}_B^B$, $\boldsymbol{\omega}_B^B$ and $\boldsymbol{v}_H^H$, $\boldsymbol{\omega}_H^H$, where those at material frames, i.e. G, require a more involved formulation described in Section 2.1.3.

As the aeroelastic wing with the hinged wing tips undergoes displacements and rotations, the hinge line vector as visualised, is a function of rigid body translational and rotational movements, and flexible deformations, and almost always a function of time. Defining instead the projections of the hinge line vector in the two local frames of reference gives $\boldsymbol{e}_H = \mathbf{R}_{HB}\boldsymbol{e}_B$, such that these vectors are now constant in time, from Euler's rotation theorem as detailed in Chapter 4.3.2 of [21].

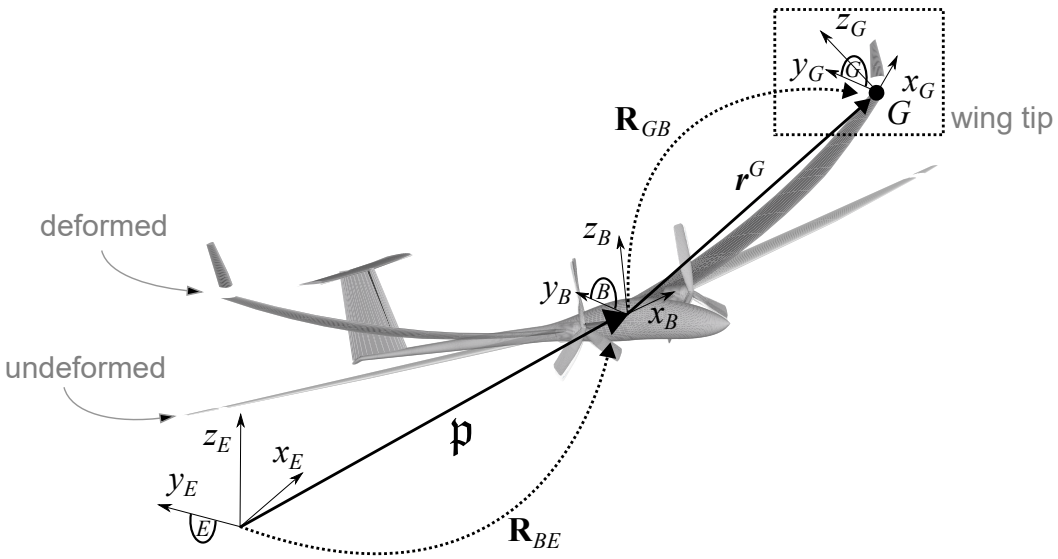

(a) Frames and notations of the wing

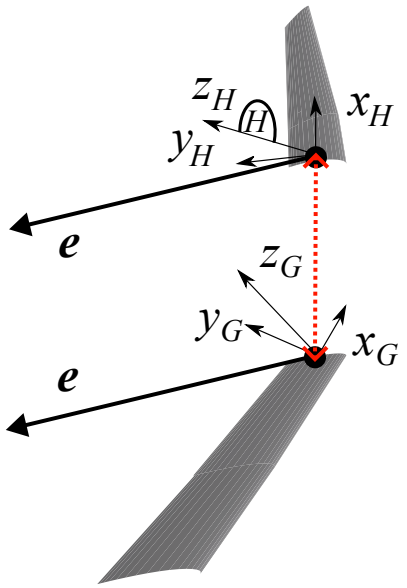

(b) Inset showing frames and notations of the wing tip

Figure 1: Labelled quantities and frames of the flexible multibody wing assembly

2.1.2 Flexible Multibody Formulation with Lagrange Multipliers

To obtain the overall structural system of equations we assemble the relevant equation of motion for each generalised DoF $\mathbf{x}$, consisting, for each of the beams within the multibody structure, the global attitude, rigid body velocities, and the flexible deformations described by displacements and rotations at the grid nodes of the beam elements, which is consistent in nomenclature as in Equation 9.4 in [21]. We then append the constraints as functions of one or several of the DoFs in the formulation. To represent the connections between different nodal DoFs and/or to address the fact that we have not explicitly chosen the DoFs to be linearly independent, we introduce extra constraint equations $\boldsymbol{g}$ which are itemised in Section 2.1.3. Multiplying with Lagrange multipliers defines an augmented Lagrangian for the system, from which we arrive at the general form of the multibody problem as

$$\begin{cases} \mathbf{M}(\mathbf{x})\ddot{\mathbf{x}} + \mathbf{B}^{\top}(\mathbf{x},\dot{\mathbf{x}},t)\boldsymbol{\lambda} = \mathfrak{f}(\mathbf{x},\dot{\mathbf{x}},t) = \mathfrak{f}_{ext}(\mathbf{x},\dot{\mathbf{x}}) - \mathfrak{f}_{gyr}(\mathbf{x},\dot{\mathbf{x}}) - \mathfrak{f}_{stif}(\mathbf{x}), \\ \boldsymbol{g}(\mathbf{x},\dot{\mathbf{x}},t) = \mathbf{B}(\mathbf{x},\dot{\mathbf{x}},t)\dot{\mathbf{x}} + \boldsymbol{g}_0 = 0 \end{cases} \tag{1}$$

in which $\mathbf{M}$ is the mass matrix and $\mathfrak{f}$ includes the external, gyroscopic, and stiffness forces respectively, and $\mathbf{B} = \frac{\partial \boldsymbol{g}}{\partial \dot{\mathbf{x}}}$ is the Jacobian of the constraints. [22] In the problems of interest, specifically with flexible hinged wing tips, $\mathfrak{f}_{ext}$ is given by a co-simulation with a UVLM solver [20,23] to give the aerodynamic forcing $\mathfrak{f}_{aero}$. If we then write Equation (1) in incremental form and recast we obtain

$$\begin{bmatrix} \mathbf{M} & 0 \\ 0 & 0 \end{bmatrix} \begin{pmatrix} \Delta\ddot{\mathbf{x}} \\ \Delta\dot{\boldsymbol{\lambda}} \end{pmatrix} + \begin{bmatrix} \mathbf{C} & \mathbf{B}^{\top} \\ \mathbf{B} & 0 \end{bmatrix} \begin{pmatrix} \Delta\dot{\mathbf{x}} \\ \Delta\boldsymbol{\lambda} \end{pmatrix} + \begin{bmatrix} \mathbf{K} & 0 \\ 0 & 0 \end{bmatrix} \begin{pmatrix} \Delta\mathbf{x} \\ 0 \end{pmatrix} = \begin{pmatrix} \mathfrak{r}^{\circ} \\ -\boldsymbol{g}^{\circ} \end{pmatrix} + \text{H.O.T.} \tag{2}$$

where the tangent damping and stiffness matrices $\mathbf{C}$ and $\mathbf{K}$, as well as the residual vector $\mathfrak{r}^{\circ}$ are given as

$$\begin{cases} \mathbf{C} = \underbrace{\dfrac{\partial \mathbf{B}^\top \boldsymbol{\lambda}}{\partial \dot{\mathbf{x}}}}_{\overline{\mathbf{C}}} - \dfrac{\partial \mathfrak{f}}{\partial \dot{\mathbf{x}}}, \\ \mathbf{K} = \dfrac{\partial (\mathbf{M}\ddot{\mathbf{x}})}{\partial \mathbf{x}} - \dfrac{\partial \mathfrak{f}}{\partial \mathbf{x}}, \\ \mathfrak{r}^\circ = \mathfrak{f} - \mathbf{M}\ddot{\mathbf{x}} - \mathbf{B}^\top \boldsymbol{\lambda} \end{cases} \tag{3}$$

evaluated at the reference point. We determine $\mathbf{B}$ for the common lower pair joints that we are interested in, then, reminding ourselves of the Newmark-β formulation for a generalised state variable $\boldsymbol{q}$,

$$\begin{cases} \boldsymbol{q}_{n+1} = \boldsymbol{q}_n + \dot{\boldsymbol{q}}_n \Delta t + (\frac{1}{2} - \beta_T)\ddot{\boldsymbol{q}}_n \Delta t^2 + \beta_T \ddot{\boldsymbol{q}}_{n+1} \Delta t^2 + \mathcal{O}(\Delta t^3), \\ \dot{\boldsymbol{q}}_{n+1} = \dot{\boldsymbol{q}}_n + (1 - \gamma_T)\ddot{\boldsymbol{q}} \Delta t_n + \gamma_T \ddot{\boldsymbol{q}}_{n+1} \Delta t^2 + \mathcal{O}(\Delta t^3). \end{cases} \tag{4}$$

Equations (2) and (4) define a well-posed linear problem. This is used to iteratively update the nonlinear equations in (1), using a predictor-corrector algorithm to accelerate convergence.

We return the converged structural solution back in nodal displacements for deforming the aerodynamic surfaces, which then the aerodynamics solver solves for the nodal loads [24], which is in turn passed onto the multibody solver for the next time step in a classical FSI coupling scheme.

The UVLM grid boundary at the hinge is skewed by the hinge axis along the flare angle - that ensures as the structure rotates about the hinge axis there is no ambiguity of the aero-structural force-displacement interface (Section 3.7 of [25]) - all UVLM grid nodes along the same chord-wise line are controlled by the displacements and rotations of the corresponding beam node. The careful choice of span-wise discretisation is hence crucial to avoid a self-intersecting UVLM grid.

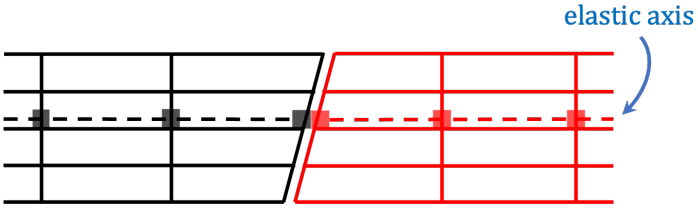

Figure 2: UVLM grid boundaries with beam nodes near the hinge

2.1.3 Multibody constraints for the hinged wing tip

Equation (1) describes the coupling of a generic flexible multibody structure; this formulation has been applied previously on other multibody systems such as wind turbines [26]. For a hinge connection between 2 beams, we require three and two equations for the linear and angular velocities respectively to allow only for one degree of freedom, which is the rotation about the hinge axis. They are derived next.

Linear velocity constraint. We begin by placing the condition of same linear velocity at frames G and H. Equating the velocities across the connection, in H frame gives

$$\boldsymbol{v}_H^H = \mathbf{R}_{HB}\left(\dot{\boldsymbol{r}}_B^G + \boldsymbol{v}_B^B + \widetilde{\boldsymbol{\omega}}_B^B \boldsymbol{r}_B^G\right), \tag{5}$$

which when written as a constraint in matrix form in the inertial frame E, and following the notation in Equation (1), is

$$\boldsymbol{g}_1 = \begin{bmatrix} -\mathbf{R}_{EB}(\chi^B) & -\mathbf{R}_{EB}(\chi^B) & \mathbf{R}_{EB}(\chi^B)\widetilde{\boldsymbol{r}}_B^G & \mathbf{R}_{EH}(\chi^H) \end{bmatrix} \begin{bmatrix} \dot{\boldsymbol{r}}_B^G \\ \boldsymbol{v}_B^B \\ \boldsymbol{\omega}_B^B \\ \boldsymbol{v}_H^H \end{bmatrix} = \mathbf{B}_1(\dot{\mathbf{x}}, \mathbf{x}, t)\dot{\mathbf{x}} = 0, \tag{6}$$

where in these expressions $\widetilde{\bullet}$ or $skew(\bullet)$ is the cross product operator. Apart from introducing the constraint as an extra equation in the system, we would also have to update the residual $\mathfrak{r}^\circ$, and evaluate $\overline{\mathbf{C}}$ in Equation (3). The only non-zero terms in the full-rank matrix $\overline{\mathbf{C}}$ are the submatrices

$$\begin{aligned} \overline{\mathbf{C}}_{\dot{\boldsymbol{r}}_B^G, \chi^B} &= -\frac{\partial}{\partial \chi^B}\left((\mathbf{R}_{EB}(\chi^B))^\top \dot{\boldsymbol{\lambda}}\right), \\ \overline{\mathbf{C}}_{\boldsymbol{v}_B^B, \chi^B} &= -\frac{\partial}{\partial \chi^B}\left((\mathbf{R}_{EB}(\chi^B))^\top \dot{\boldsymbol{\lambda}}\right), \\ \overline{\mathbf{C}}_{\boldsymbol{\omega}_B^B, \chi^B} &= \frac{\partial}{\partial \chi^B}\left((\mathbf{R}_{EB}(\chi^B))^\top \left(\widetilde{\boldsymbol{r}}_B^G \dot{\boldsymbol{\lambda}}\right)\right), \\ \overline{\mathbf{C}}_{\boldsymbol{v}_H^H, \chi^H} &= \frac{\partial}{\partial \chi^H}\left((\mathbf{R}_{EB}(\chi^H))^\top \dot{\boldsymbol{\lambda}}\right). \end{aligned} \tag{7}$$

As our constraint matrix $\mathbf{B}_1$ in Equation (6) is a function of the generalised displacement we have an extra contribution to the tangent stiffness matrix $\mathbf{K}$ not yet included in Equation (3)

$$\Delta\mathbf{K} = \underbrace{\frac{\partial \mathbf{B}^\top \dot{\boldsymbol{\lambda}}}{\partial \mathbf{x}}}_{\overline{\mathbf{K}}} \tag{8}$$

which when evaluated gives

$$\overline{\mathbf{K}}_{\boldsymbol{\omega}_B^B, \boldsymbol{r}_B^G} = -\mathbf{R}_{EB}(\chi^B)\widetilde{\dot{\boldsymbol{\lambda}}} \tag{9}$$

Angular velocity constraint. To apply the angular velocity constraint, in practice we restrict any two pairs of corresponding points on the vectors to always have the same linear velocity. Choosing the origins of the vectors in Figure 1b as the first pair gives Equation (5), and additionally choosing two points along the vectors give their common linear velocity in the H frame as

$$\boldsymbol{v}_H^H + \widetilde{\boldsymbol{\omega}}_H^H \boldsymbol{e}_H = \mathbf{R}_{HB}\left(\dot{\boldsymbol{r}}_B^G + \boldsymbol{v}_B^B + \widetilde{\boldsymbol{\omega}}_B^B \boldsymbol{r}_B^G\right) + \mathbf{R}_{HG}(\text{skew}(\mathbf{T}^{GB}\dot{\boldsymbol{\psi}}_B^G + \mathbf{R}_{GB}\boldsymbol{\omega}_B^B)\boldsymbol{e}_B), \tag{10}$$

where $\mathbf{T}$ is the tangential rotational operator described in Appendix C of [21], from which we eliminate Equation (5) to give

$$\widetilde{\boldsymbol{\omega}}_H^H \boldsymbol{e}_H = \mathbf{R}_{HG}(\text{skew}(\mathbf{T}^{GB}\dot{\boldsymbol{\psi}}_B^G + \mathbf{R}_{GB}\boldsymbol{\omega}_B^B)\boldsymbol{e}_B), \tag{11}$$

which is transformed to G frame and recast as

$$\boldsymbol{g}_2 = \mathbf{R}_{GB}\mathbf{R}_{BE}\mathbf{R}_{EH}\widetilde{\boldsymbol{\omega}}_H^H \boldsymbol{e}_H + \widetilde{\boldsymbol{e}}_B(\mathbf{T}^{GB}\dot{\boldsymbol{\psi}}_B^G + \mathbf{R}_{GB}\boldsymbol{\omega}_B^B) = 0, \tag{12}$$

and in matrix form,

$$\boldsymbol{g}_2 = \begin{bmatrix}\widetilde{\boldsymbol{e}}_B\mathbf{R}_{GB}(\boldsymbol{\psi}_B^G) & \widetilde{\boldsymbol{e}}_B\mathbf{T}^{GB}(\boldsymbol{\psi}_B^G) & -\mathbf{R}_{GB}(\boldsymbol{\psi}_B^G)\mathbf{R}_{BE}(\chi^B)\mathbf{R}_{EH}(\chi^H)\widetilde{\boldsymbol{e}}_H\end{bmatrix}\begin{bmatrix}\boldsymbol{\omega}_B^B \\ \dot{\boldsymbol{\psi}}_B^G \\ \boldsymbol{\omega}_H^H\end{bmatrix} = \mathbf{B}_2(\dot{\mathbf{x}}, \mathbf{x}, t)\dot{\mathbf{x}} = 0. \tag{13}$$

We then follow a similar procedure as in Section 2.1.3 to obtain $\overline{\mathbf{C}}$ and $\overline{\mathbf{K}}$,

$$\begin{aligned}
\overline{\mathbf{K}}_{\boldsymbol{\omega}_B^B,\boldsymbol{\psi}_B^G} &= -\frac{\partial(\mathbf{R}_{GB}(\boldsymbol{\psi}_B^G))^\top}{\partial\boldsymbol{\psi}_B^G}(\widetilde{\boldsymbol{e}}_B\dot{\boldsymbol{\lambda}}), \\
\overline{\mathbf{K}}_{\dot{\boldsymbol{\psi}}_B^G,\boldsymbol{\psi}_B^G} &= -\frac{\partial(\mathbf{T}(\boldsymbol{\psi}_B^G))^\top}{\partial\boldsymbol{\psi}_B^G}(\widetilde{\boldsymbol{e}}_B\dot{\boldsymbol{\lambda}}), \\
\overline{\mathbf{K}}_{\boldsymbol{\omega}_H^H,\boldsymbol{\psi}_B^G} &= \widetilde{\boldsymbol{e}}_H\mathbf{R}_{HE}(\chi^H)\mathbf{R}_{EB}(\chi^B)\frac{\partial(\mathbf{R}_{BG}(\boldsymbol{\psi}_B^G))}{\partial\boldsymbol{\psi}_B^G}\dot{\boldsymbol{\lambda}}, \\
\overline{\mathbf{C}}_{\boldsymbol{\omega}_H^H,\chi^B} &= \widetilde{\boldsymbol{e}}_H\mathbf{R}_{HE}(\chi^H)\frac{\partial\mathbf{R}_{EB}(\chi^B)}{\partial\chi^B}(\mathbf{R}_{BG}(\boldsymbol{\psi}_B^G)\dot{\boldsymbol{\lambda}}), \\
\overline{\mathbf{C}}_{\boldsymbol{\omega}_H^H,\chi^H} &= \widetilde{\boldsymbol{e}}_H\frac{\partial\mathbf{R}_{HE}(\chi^H)}{\partial\chi^H}(\mathbf{R}_{EB}(\chi^B)\mathbf{R}_{BG}(\boldsymbol{\psi}_B^G)\dot{\boldsymbol{\lambda}}).
\end{aligned} \tag{14}$$

2.1.4 Trimming procedure

In general, a flexible aircraft is trimmed by subsequent static computations of deformed geometry and load subjected to control inputs, which are given by a gradient based method as a function of previous total forces and moments on the system. Loosely speaking, when dealing with the relatively simple case of longitudinal trim, we can associate input-output systems of primary importance by physical arguments - lift is mostly influenced by angle of attack, drag by thrust, and pitching moment by elevator deflection.

For a flexible aircraft with flared hinged wing, the mechanism at the hinge renders the static approach challenging - an alternative method is required to obtain cheaper dynamic equilibria of the multibody system. By replacing the gradient based approach with independent single-input single-output (SISO) control systems loosely coupled by the nonlinear aeroelastic dynamics, we provide the multibody system with natural damping to promote convergence when time-stepping the solution. In the case of longitudinal trim, we have clamped the otherwise free-flying aircraft except the pitching degree of freedom (as it is the only necessary DoF), and set up 3 PI controllers for lift-angle of attack, drag-thrust, pitching moment-elevator relationships for zero targets for all measured forces and moments, as will be shown in Section 3.2.

3 VERY FLEXIBLE AIRCRAFT

With our verified formulation we now shift our focus to the modelling and analysis of a representative High-Altitude Long-Endurance (HALE) T-tail-configured aircraft, which has been previously used to investigate dynamic aeroelasticity in reduced-order modelling, nonlinear control, wake vortex encounters, maneuvres, amongst others [27, 28]. In the subsequent analyses we have not applied any sectional correction for the lift and drag obtained from the UVLM solution, which in most cases will give us a conservative estimate of loads and displacements and likely system dynamics.

3.1 HALE and H^{2}ALE aircraft models

The HALE aircraft, as shown in Figure 3, is configured with a constant-chord, unswept wing of aspect ratio $= 32$ and a T-tail, powered by a constant thrust force in the material frame forward direction at $\pm 1m$ spanwise from the wing/fuselage intersection, and trimmed for longitudinal flight by means of an elevator deflection input. The flexible wing weighs $24\,\mathrm{kg}$; the rest of the structure weighs $54.25\,\mathrm{kg}$, $50\,\mathrm{kg}$ of which is a lumped mass at the wing-fuselage intersection. The numerical model is made parametric with respect to the dihedral angle of the wing tips, with versions denoted as HALE-dXX where XX is the dihedral angle in degrees. More details on the architecture of the model can be found in [29].

Based on the HALE aircraft model we have built the H^{2}ALE by replacing the dihedral seen at the outboard sections of the wings with a pair of flared hinged wing tips. The wing tips are allowed to flap freely and constitute one-fourth of the total span, which should be more than sufficient for the wing-wing tip interactions to be evident [16]. The numerical model is made parametric with respect to the flare angle, with versions denoted as H^{2}ALE-fXX where XX is the flare angle β in degrees. Figure 4 shows the H^{2}ALE aircraft in steady level flight, where as the flare angle increases, the equilibrium fold angle decreases, while bending/twisting of the main wing increases.

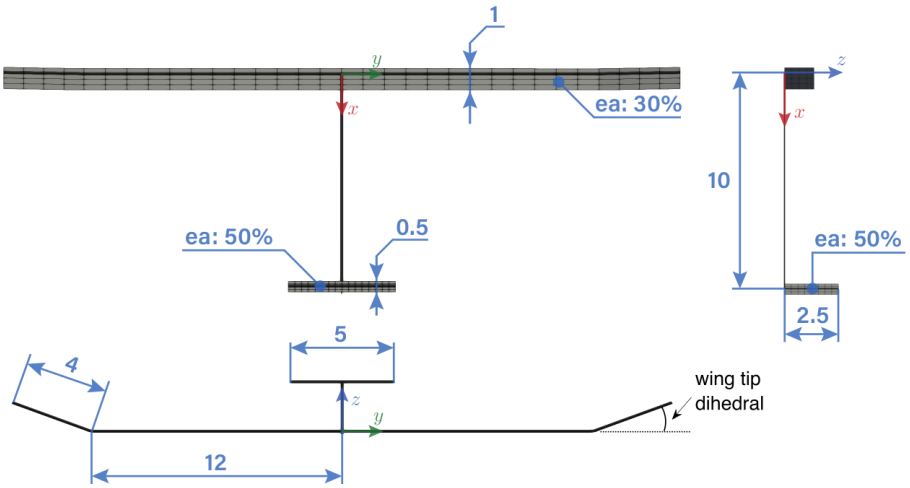

Figure 3: Geometric definition of the T-tail HALE model with all units in meters as in [29].

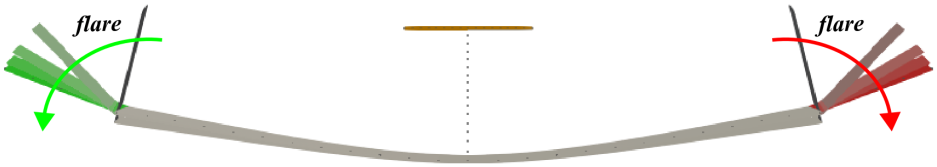

Figure 4: H^{2}ALE aircraft, with flared hinged wing tips coloured in increasing flare, at trim

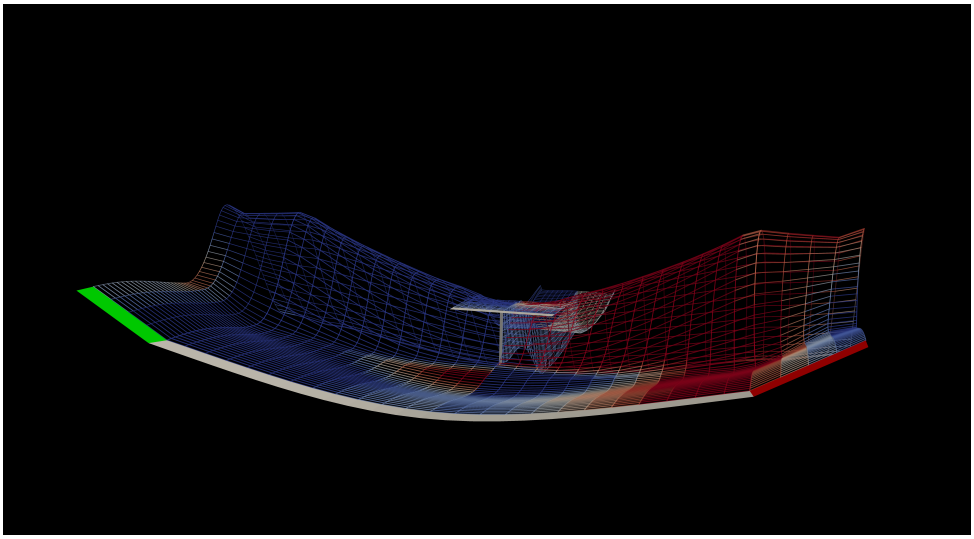

Figure 5: H^{2}ALE-f10 during a vertical gust encounter, with force-free UVLM wake grid coloured by circulation intensity

We have first selected the HALE-d00 and the HALE-d90, to compare with the H^{2}ALE-f10 - it is thought that the former configurations would be good proxies of the latter with the flared hinged wing tips locked. A small flare angle of 10 degrees is shown to be enough practically for ensuring the dynamic stability of the hinged wing tips, while having a larger flare angle would extend the stability boundary with respect to sideslip angle [8], but lead to lower damping in the hinge flapping mode. Fundamentally, the H^{2}ALE will have the locked, stretched out (HALE-d00) and folded up (HALE-d90) configurations as limit cases - its dynamics is shown in subsequent sections to mostly fall in between that of the two references.

3.2 Aeroelastic trim and equilibrium state

We first perform trimming of the three aircraft at a flow velocity of $10\,\mathrm{m\,s^{-1}}$. respectively with the algorithm described in Section 2.1.4. The time histories of the control inputs versus corresponding states are shown in Figure 6.

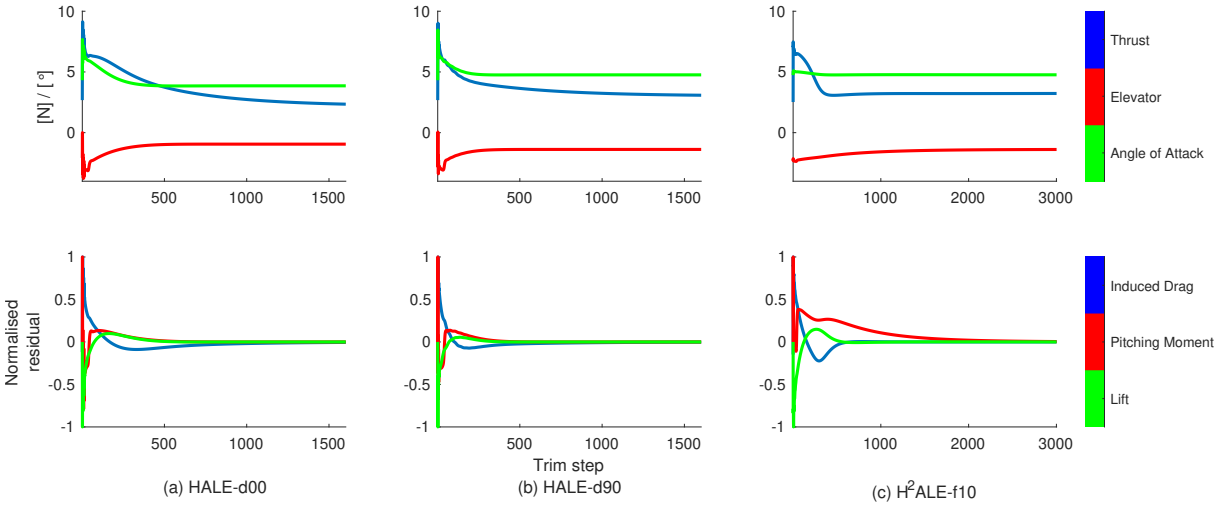

Figure 6: Trim time histories of control input versus corresponding states

The longitudinal trim values are given in Table 1. We have nondimensionalised the pitching moment and lift by weight multiplied by chord, and weight, respectively. Do note the residual induced drag here, as percentage of thrust, is secondary to the elevator and angle of attack inputs - the thrust only ensures the aircraft is in equilibrium longitudinally.

Both the HALE-d90 and H^{2}ALE-f10 requires a slightly higher angle of attack for longitudinal trim - that is thought to be a result of the partial loss in lift outboard of the hinge, resulting in a higher angle of incidence at the main wing to generate the same overall lift. Elevator and thrust input is likewise higher in magnitude to counteract the extra pitching moment and induced drag due to the higher angle of attack.

Table 1: Comparison of trimmed values for HALE and H^{2}ALE

Values at trim	HALE-d00	HALE-d90	H^{2}ALE-f10
Thrust [N]	2.35	3.08	3.23
Residual Induced Drag [%]	13.1	4.10	0.27
Elevator [deg]	-0.95	-1.38	-1.39
Residual Pitching Moment [%]	0.00	0.00	0.14
Angle of attack [deg]	3.86	4.76	4.76
Residual Lift [%]	0.00	0.00	0.03

3.3 Vertical gust response

To understand more about the coupled flight dynamics and aeroelastics, we have performed a gust length sensitivity analysis by subjecting each of the three aircraft from their respective trim state defined in Section 2.1.4 to 1-cos gusts across an order of magnitude in length centered around the vehicle length (10 m), and constant intensity of 50% u_{inf}. It is hoped that the gust will then excite the combination of aeroelastics and flight dynamics at different length and time scales, allowing for a comparison of the responses. The tracked variable, wing root bending moment, is chosen because it is thought to be the most critical in a vertical gust encounter. It is nondimensionalised using the product of the aircraft weight and one-eighth span length (4

m). As shown in Figure 7, the H^{2}ALE-f10 has a trim WRBM between the two HALE configurations as predicted, with value much closer to that of HALE-d90 - that implies with the free flared hinge we can almost recover the best case scenario of vertical winglets in terms of alleviating the bending loads at the root.

In terms of the sensitivities, the HALE configurations show a early peak in response, both at the 7.5 m mark, where the H^{2}ALE-f10 peaks at 15 m, suggesting different mechanisms in play especially after the first WRBM peak in response to the gust. We have chosen to compare the gust intensity sweep, from 0 to 160% u_{inf}, of the three configurations, at the latter of the identified gust length since it is biased against the H$^2ALE-f10$ for a conservative comparison. We have intentionally chosen high values for the gust intensity, both to examine the dynamics of the very flexible aircraft configurations at extreme geometric nonlinearities, and to demonstrate robustness of the numerical implementation.

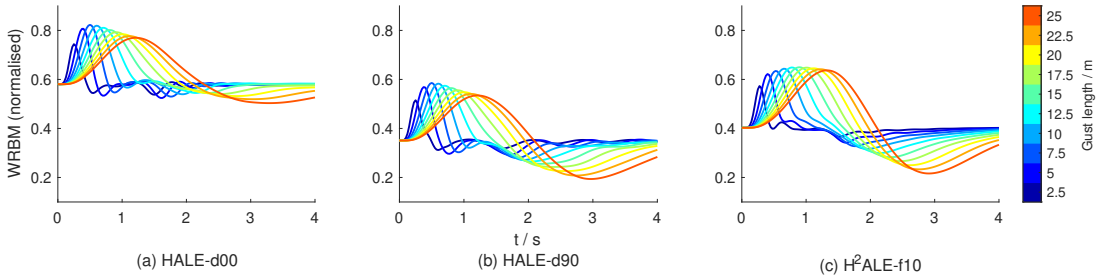

Figure 7: Time histories of nondimensionalised wing root bending moment at various gust lengths, gust intensity = 50% u_{inf}

3.3.1 Gust length = 15 m

This is the most sensitive gust length for the H^{2}ALE-f10 - as evidenced by Figure 8, where the transient WRBM increment due to the longitudinal gust is consistently higher than the HALE configurations. However, comparing the total 1g+gust dimensional WRBM seen, both the HALE-d00 and HALE-d90 still experience higher maximum transient WRBM than the H^{2}ALE-f10 at the highest gust intensity of 160% u_{inf}. The transient oscillations are qualitatively more damped than both the HALE-d00 and HALE-d90 with the H^{2}ALE, suggesting the hinge is helpful in this particular setup and conditions to alleviate the oscillating gust loads. It is worth noting that the WRBM increments as plotted do not exactly coincide as the gust intensity increases - this is because of the geometric nonlinearities captured in the formulation. That leads to another silver lining to this identified, since the hinge mechanism results in progressively less WRBM when increasing gust intensity, i.e. nonlinear load relief.

Examining the wing root torsional and bending moment plotted against each other in Figure 9 reveals a few trends - first of all, that the H^{2}ALE-f10 shares similar correlation of bending to torsional loads with the HALE-d00, and that they are much less coupled than in HALE-d90, where the fixed vertical wing tips act as unbalanced OOP masses promoting bending-twisting coupling. In terms of the magnitude of loads experienced, the H^{2}ALE sees loads comparable to the HALE-d90 and significantly smaller than HALE-d00.

In determining the load envelope of a particular aircraft configuration Figure 9 also demon-

strates why it is important to consider the nonlinear dynamics - for the H^{2}ALE-f10, and to a lesser extent the HALE-d90, the largest gust intensity case does not define the entire load envelope.

In addition to the zero moment transfer, a second mechanism of wing root bending moment relief is seen for the H^{2}ALE. At gust onset the inner wing tends to fly up and flex up, and through the hinge by inertia and aerodynamic damping the wing tips tend to fold negatively (seen in Figure 10) - that leads to higher effective angle of attack on the wing tips due to the downwards flapping motion, and higher geometric angle of attack on the wing tips due to flare. These combined gives upwards (restoring) lift on the wingtips (which as the gust intensity increases the higher frequency flapping modes become less damped - becoming a potential source of LCO in the wing assembly), and hence a downwards (dampening) force is exerted through the hinge on the inner wing, reducing the flex up tendency, itself a self-regulating cycle which in time dampens any transient flexible and hinge motion, as evidenced by Figure 11. Note also the WRBM and z are almost always in phase, suggesting one is a good proxy for the other, in this largely inertia-driven wing tip assembly. Indeed in terms of the flexible deformation the H^{2}ALE-f10 enjoys the best of both worlds - quicker to settle to equilibrium shape than the HALE-d00, and much more damped oscillations than the HALE-d90, likely due to the dissipative flapping identified earlier.

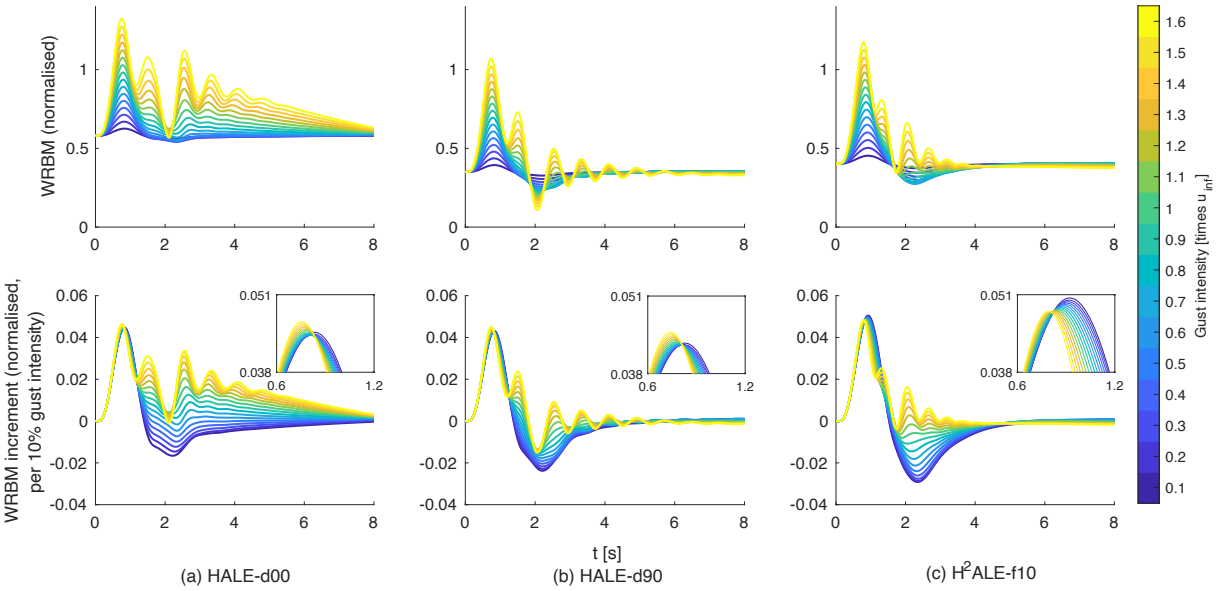

Figure 8: Time histories of normalised and incremental WRBM over range of gust intensities, gust length = 15 m. Moment increment plots include inset with values near the first peak.

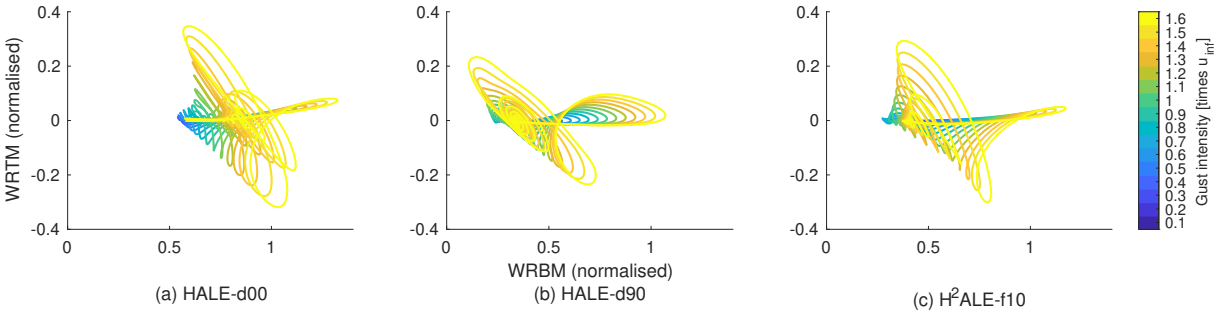

Figure 9: Instantaneous values of normalised wing root bending and torsional moment over range of gust intensities, gust length = 15 m

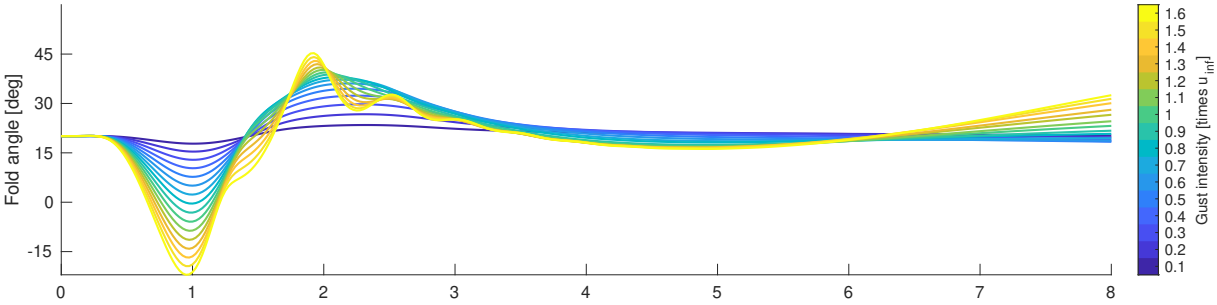

Figure 10: Time histories of hinge fold angle for the H^{2}ALE-f10, gust length = 15 m

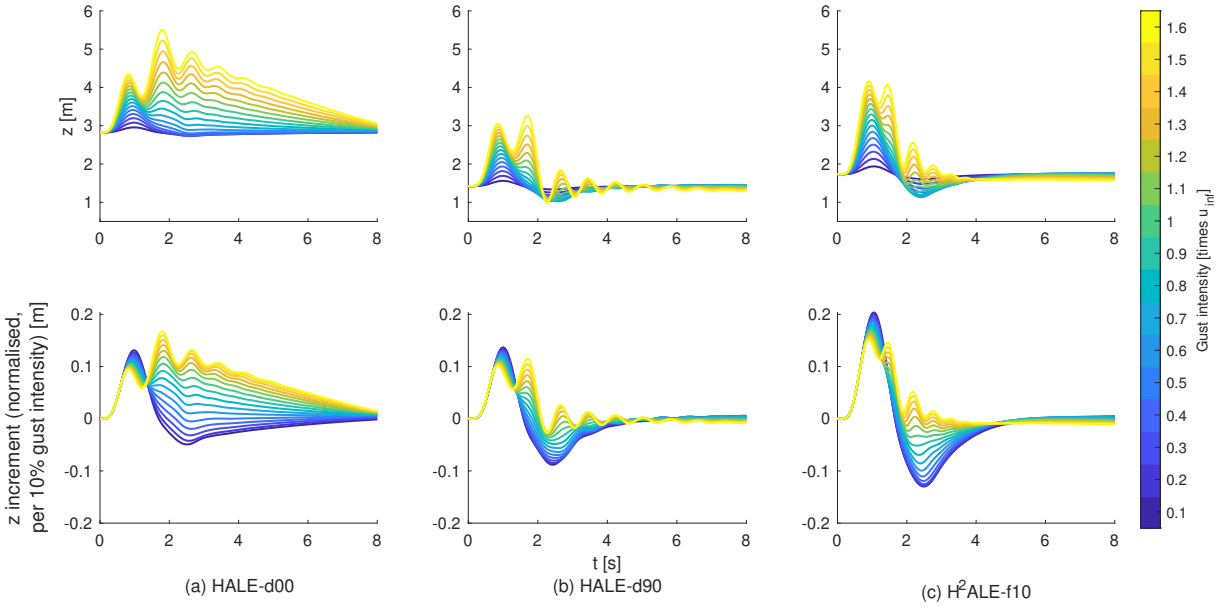

Figure 11: Time histories of wing dihedral/hinge vertical position relative to root over range of gust intensities, gust length = 15 m

3.4 Lateral gust response

The lateral gust response, at least for the H^{2}ALE, is driven by quite different physics when compared to the vertical gust response. A 1-cos lateral gust to the right wing (starboard side)

is applied to all of the configurations. It is thought that the wing tip collision at fold angle $= \pm 180°$ should be used as the sizing case rather than WBRM as in the vertical gust case - hence in Figure 12 we plot the evolution of the fold angle with gust length.

The first peak in the starboard fold angle levels off with respect to the gust length. It is thought that it is due to the wing tip dynamics induced by the lateral gust since the subsequent rigid body (roll) dynamics, identified by the time scales, scale with gust length.

We have chosen gust length $= 15$ m as before for a reasonable range of fold angle, as well as a good mix of wing tip and rigid body driven flight dynamics. The intensity sweep is limited to a maximum of 60% u_{inf} to prevent unwanted wake defects causing numerical issues in the time marching simulations.

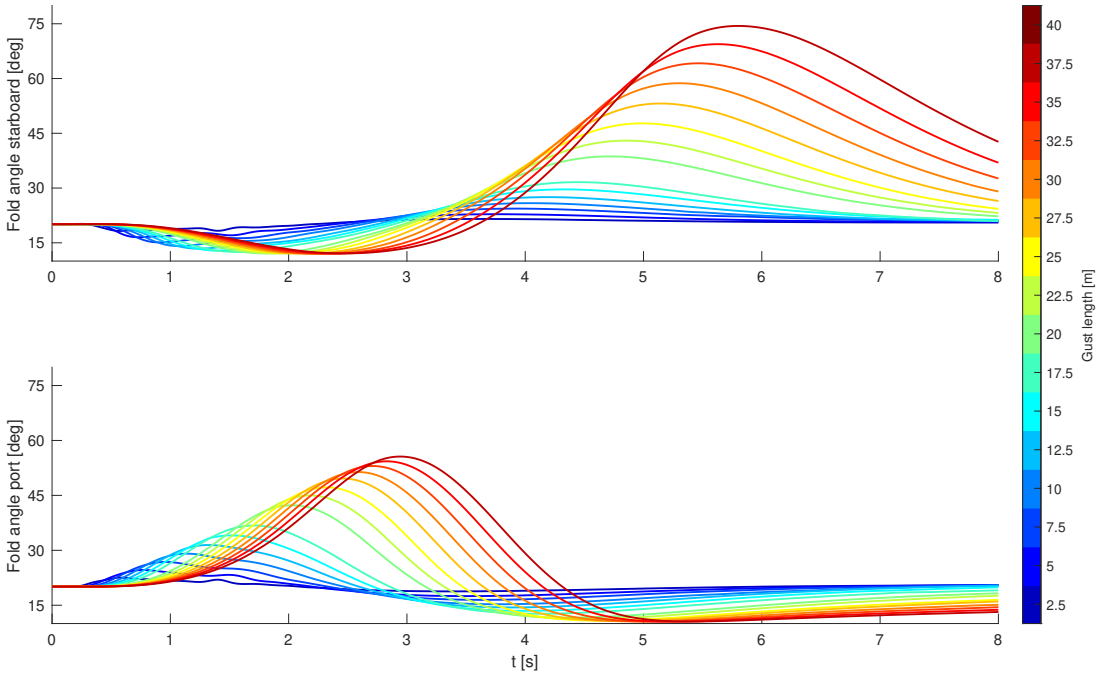

Figure 12: Time histories of hinge fold angle port and starboard at various lateral gust lengths, gust intensity = 50% u_{inf}

We have plotted all the Euler angles (roll Φ, pitch Θ, and yaw Ψ) and their time derivatives in Figure 13 - as the aircraft is in steady level flight before the gust hits all parameters other than Θ begin at 0, and that Θ at trim is dependent on the aircraft configuration.

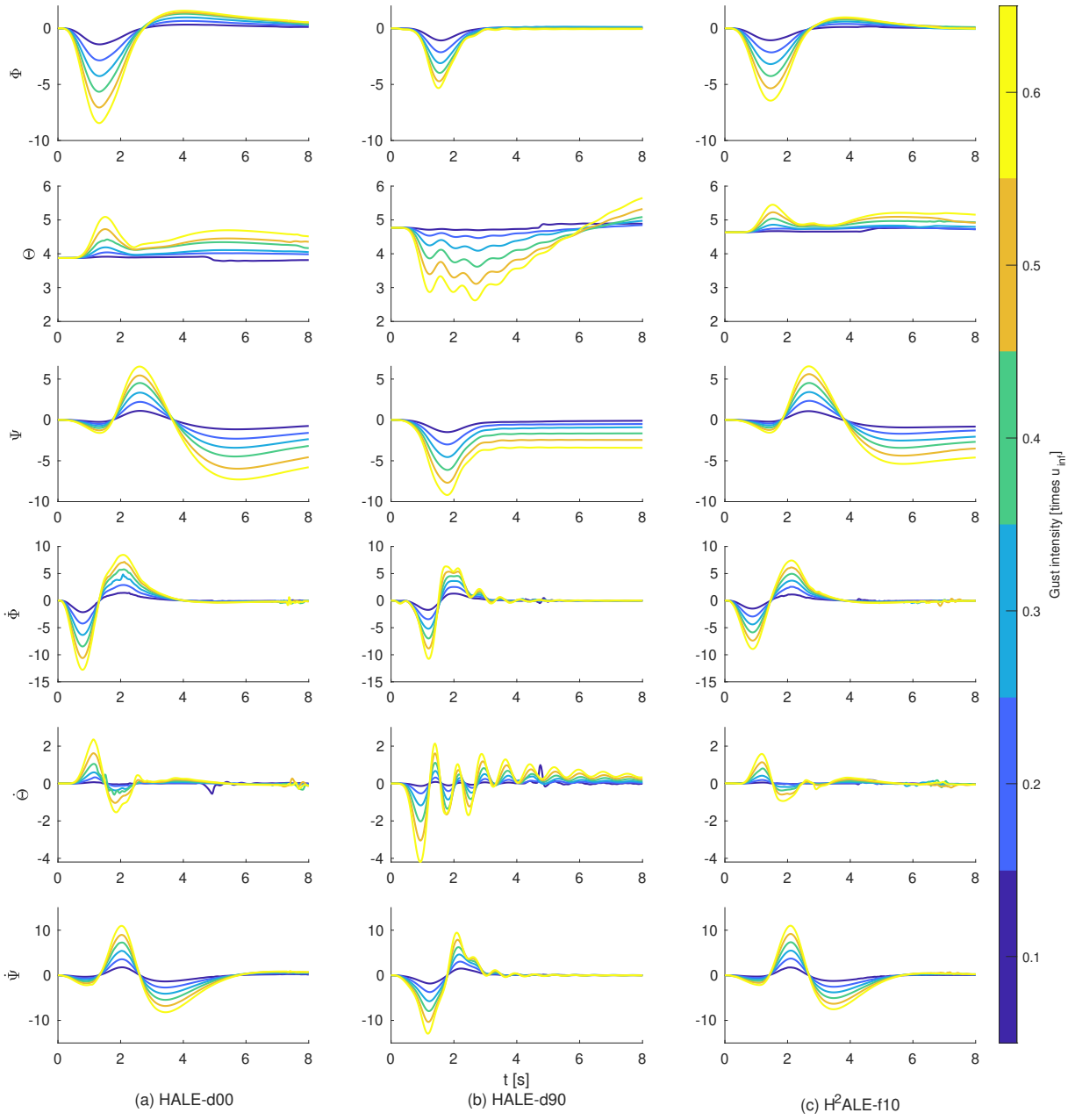

Figure 13: Time histories of Euler angles in degrees and their derivatives over range of gust intensities, lateral gust length = 15 m

Comparing the roll angle response we'll find the HALE-d90 has the highest roll stability out of the three, whereas the HALE-d00 reached the highest roll angle. Comparing then the roll rates gives a different story - for the first peak the H^{2}ALE-f10 showed the lowest angular roll velocity across gust intensity levels amongst the three configurations, indicating a higher roll damping, perhaps akin to the vertical gust scenario where we have lower increments in WRBM with increasing gust intensity. These can both be attributed to the flapping motion allowing for dissipation.

The pitch angle and the time derivative show a similar trend where H^{2}ALE-f10 has smaller magnitudes than the HALE-d00. The HALE-d90 demonstrates fundamentally different physics

- as the aircraft rolls there is a tendency to pitch down rather than up, and it yaws in the different direction (right wing aft) as the plane banks right - which indicates the worsening spiral mode characteristics with the fixed-upwards wing tips.

Time histories of the yaw angle and its derivative remains constant across HALE-d00 and H^{2}ALE-f10 - suggesting in the flight dynamics timescale the free wing tips has a negligible impact at least in the directional flight characteristics.

From the time histories of the port and starboard fold angles in Figure 15, it is perhaps interesting to see the fold angle histories are approximately in the same timescale as the roll angle history - the wing tips in H^{2}ALE-f10 are the first to react to the gust, and is subsequently driven by the inertial of the wingtips and flight dynamics - at the gust encounter, the positive-y forcing on the each of the wing tips pushes the starboard tip down and port tip up - and because the hinge moment imparted by the aerodynamic force increase with fold angle up to $\pm 90^\circ$ due to geometry, port fold angle magnitudes are higher. They then reverse direction as the restoring motion from the flight dynamic modes dominate.

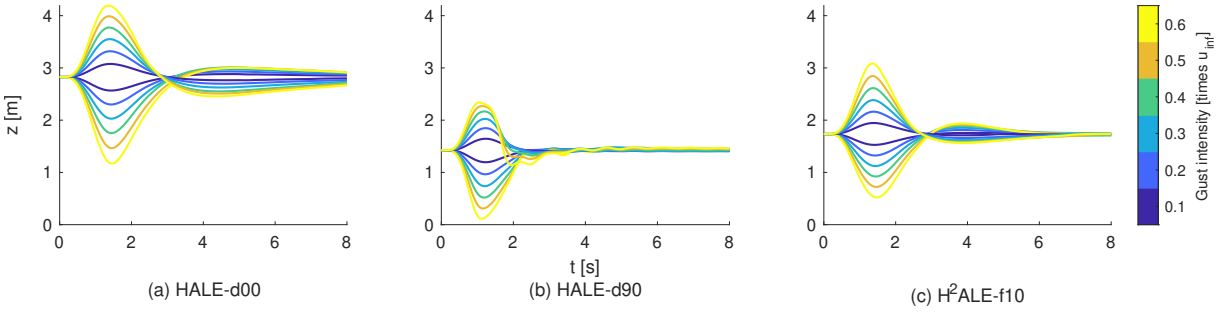

Figure 14: Time histories of wing dihedral/hinge vertical positions port and starboard, relative to root, over range of gust intensities, lateral gust length = 15 m

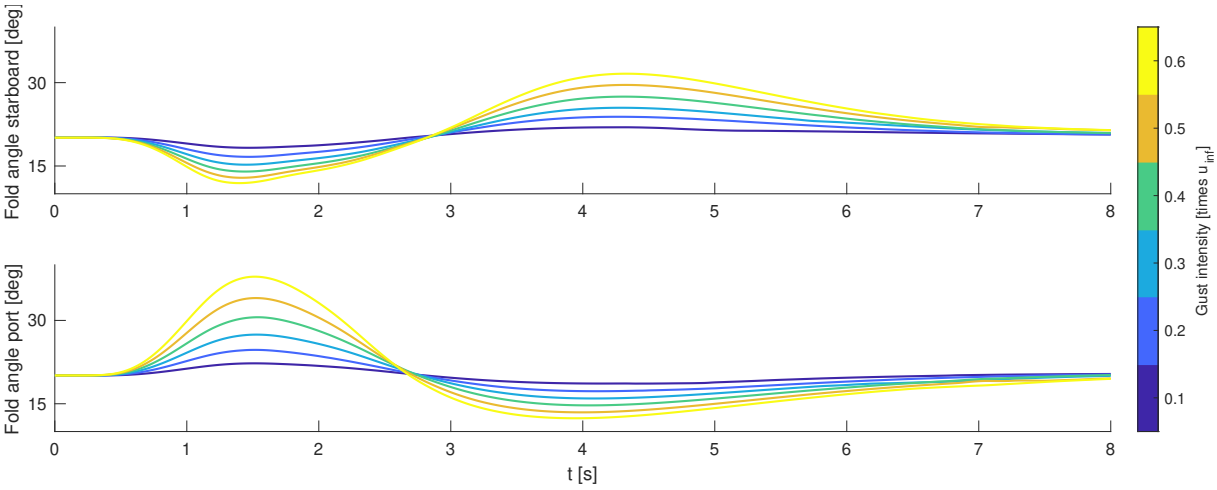

Figure 15: Time histories of hinge fold angle for H^{2}ALE-f10 port and starboard, relative to root, over range of gust intensities, lateral gust length = 15 m

4 CONCLUSION

In this work we have presented the methodology in modelling the flexible multibody flared hinged wing, and set up the simulation of a High-Altitude Long-Endurance (HALE) T-tail aircraft. A representative model featuring flared hinged wing tips, H^{2}ALE, is proposed, which is based on a previous HALE aircraft model. Aeroelastic trim and equilibrium states are computed for both models with converged respective control inputs. A vertical gust sweep in length and intensity, and subsequently a lateral gust sweep in intensity, is performed on three HALE and H^{2}ALE subconfigurations to better understand the coupled aeroelastics and flight dynamics in play.

In terms of the static wing root bending load alleviation in vertical gust, this is shown to be primarily a feature of the hinge mechanism - and is a weak function of all other variables. Notably, the WRBM of all H^{2}ALE subconfigurations closely approach the HALE-90, i.e. the fixed upturned wing tip case, demonstrating exceptional efficiency. As for the dynamic load alleviation in vertical gust, the HALE is most sensitive to the shorter gust length 7.5 m, while the H^{2}ALE the longer 15 m. At higher gust lengths the incremental H^{2}ALE response can be the most severe out of the three compared configurations, but the 1g+gust response remains bounded by the HALE-d00 and the HALE-d90, a trend which is seen across different variables investigated. A comparison of the first positive (wing tip up) peak increment loads normalised by gust intensity shows that the increment on H^{2}ALE is slightly larger than the HALE cases, but there are nonlinear effects at higher gust intensities that the H^{2}ALE only can leverage to reduce the increments.

The performance of H^{2}ALE in lateral gusts are constrained by the fold angle - we would like to avoid the wing tips flipping and striking the main wing. Across gust intensities in a lateral gust encounter the H^{2}ALE-f10 shows maximum instantaneous roll angle attained as proxy for roll stability in between the two HALE configurations, and maximum time derivative of roll angle as proxy for roll damping the highest amongst the three configurations. The roll dynamics are mostly coupled with pitching, where yaw seen in H^{2}ALE-f10 seems unaffected at all by the addition of the hinge and is virtually identical to that of HALE-d00, whilst a fundamentally difference response is seen in the HALE-d90.

Future work will include expanding the investigation to the impact of flare angle, as well as wing tip mass and stiffness distribution on the nonlinear response, then subsequently the application of the aforementioned formulation to a representative next-generation aircraft model with and without flared hinged wing tips, to uncover the nonlinear dynamics which will inform the exploration of the nonlinear aeroelastic design space of aircraft with such wing assemblies across a range of operating conditions.

5 REFERENCES

[1] ATI (2022). Destination Zero - The Technology Journey to 2050. *ATI Technology Strategy 2022 - Destination Zero*. ISSN 00317217.

[2] Wunderlich, T. F., Dähne, S., Reimer, L., et al. (2021). Global aerostructural design optimization of more flexible wings for commercial aircraft. *Journal of Aircraft*, 58(6). ISSN 15333868. doi:10.2514/1.C036301.

[3] Miceli, M. F., Ameduri, S., Dimino, I., et al. (2023). A Preliminary Technology Readiness Assessment of Morphing Technology Applied to Case Studies. *Biomimetics*, 8(1). ISSN 23137673. doi:10.3390/biomimetics8010024.

[4] Ameduri, S. and Concilio, A. (2023). Morphing wings review: aims, challenges, and current open issues of a technology. *Proceedings of the Institution of Mechanical Engineers, Part C: Journal of Mechanical Engineering Science*, 237(18). ISSN 20412983. doi:10.1177/0954406220944423.

[5] Castrichini, A., Wilson, T., Saltari, F., et al. (2020). Aeroelastics Flight Dynamics Coupling Effects of the Semi-Aeroelastic Hinge Device. *Journal of Aircraft*, 57(2), 333–341. ISSN 1533-3868. doi:10.2514/1.C035602.

[6] Wilson, T., Castrichini, A., Azabal, A., et al. (2017). Aeroelastic Behaviour of Hinged Wing Tips. In *International Forum on Aeroelasticity and Structural Dynamics, IFASD 2017*. Como, Italy.

[7] Castrichini, A., Siddaramaiah, V. H., Calderon, D., et al. (2017). Preliminary investigation of use of flexible folding wing tips for static and dynamic load alleviation. *The Aeronautical Journal*, 121(1235), 73–94. ISSN 0001-9240. doi:10.1017/aer.2016.108.

[8] Conti, C., Saltari, F., Mastroddi, F., et al. (2021). Quasi-Steady Aeroelastic Analysis of the Semi-Aeroelastic Hinge Including Geometric Nonlinearities. *Journal of Aircraft*, 58(5), 1168–1178. ISSN 1533-3868. doi:10.2514/1.C036115.

[9] Mastracci, P., Saltari, F., Mastroddi, F., et al. (2022). Unsteady Aeroelastic Analysis of the Semi Aeroelastic Hinge Including Local Geometric Nonlinearities. *AIAA Journal*, 60(5), 3147–3165. ISSN 0001-1452. doi:10.2514/1.J061108.

[10] Balatti, D., Khodaparast, H. H., Friswell, M. I., et al. (2023). Experimental and numerical investigation of an aircraft wing with hinged wingtip for gust load alleviation. *Journal of Fluids and Structures*, 119, 103892. ISSN 08899746. doi:10.1016/j.jfluidstructs.2023.103892.

[11] Cheung, R. C. M., Rezgui, D., Cooper, J. E., et al. (2020). Testing of Folding Wingtip for Gust Load Alleviation of Flexible High-Aspect-Ratio Wing. *Journal of Aircraft*, 57(5), 876–888. ISSN 1533-3868. doi:10.2514/1.C035732.

[12] Healy, F., Cheung, R., Rezgui, D., et al. (2023). On the Effect of Geometric Nonlinearity on the Dynamics of Flared Folding Wingtips. *Journal of Aircraft*, 60(2), 368–381. ISSN 0021-8669. doi:10.2514/1.C036877.

[13] Healy, F., Rezgui, D., and Cooper, J. E. (2023). Experimental Effect of Sideslip Angle on the Dynamic Behaviour of Flared Folding Wingtips. In *AIAA SCITECH 2023 Forum*. Reston, Virginia: American Institute of Aeronautics and Astronautics. ISBN 978-1-62410-699-6. doi:10.2514/6.2023-0376.

[14] Carrillo Córcoles, X., Mertens, C., Sciacchitano, A., et al. (2023). Effect of Wing Stiffness and Folding Wingtip Release Threshold on Gust Loads. *Journal of Aircraft*, 1–20. ISSN 0021-8669. doi:10.2514/1.C037108.

[15] Healy, F., Cheung, R., Rezgui, D., et al. (2023). Experimental and Numerical Nonlinear Stability Analysis of Wings Incorporating Flared Folding Wingtips. *Journal of Aircraft*, 1–15. ISSN 0021-8669. doi:10.2514/1.C037167.

[16] Cooper, J. E., Gu, H., Ricci, S., et al. (2024). CS2-THT U-HARWARD Project: Final Assessment and Project Outcomes Evaluation. In *AIAA SCITECH 2024 Forum*. Reston, Virginia: American Institute of Aeronautics and Astronautics. ISBN 978-1-62410-711-5. doi:10.2514/6.2024-2111.

[17] Gu, H., Healy, F., Constantin, L., et al. (2024). Aeroelastic Scaling of a High-Aspect-Ratio Wing Incorporating a Semi-Aeroelastic Hinge. *AIAA Journal*, 1–13. ISSN 0001-1452. doi:10.2514/1.J063646.

[18] Healy, F., Cheung, R., Neofet, T., et al. (2022). Folding Wingtips for Improved Roll Performance. *Journal of Aircraft*, 59(1), 15–28. ISSN 1533-3868. doi:10.2514/1.C036372.

[19] Sanghi, D., Cesnik, C. E. S., and Riso, C. (2024). Roll Maneuverability of Transonic High-Aspect-Ratio-Wing Aircraft with Flared Folding Wingtips. *Journal of Aircraft*, 1–14. ISSN 0021-8669. doi:10.2514/1.C037470.

[20] del Carre, A., Muñoz-Simón, A., Goizueta, N., et al. (2019). SHARPy: A dynamic aeroelastic simulation toolbox for very flexible aircraft and wind turbines. *Journal of Open Source Software*, 4(44), 1885. ISSN 2475-9066. doi:10.21105/joss.01885.

[21] Palacios, R. and Cesnik, C. E. S. (2023). *Dynamics of Flexible Aircraft*. Cambridge University Press. ISBN 9781108354868. doi:10.1017/9781108354868.

[22] Bauchau, O. A. (2011). *Flexible Multibody Dynamics*, vol. 176. Dordrecht [u.a.]: Springer. ISBN 9789400703346.

[23] Düssler, S. and Palacios, R. (2024). Enhanced Unsteady Vortex Lattice Aerodynamics for Nonlinear Flexible Aircraft Dynamic Simulation. *AIAA Journal*, 62(3), 1179–1194. ISSN 0001-1452. doi:10.2514/1.J063174.

[24] Düssler, S., Goizueta, N., Muñoz-Simón, A., et al. (2022). Modelling and Numerical Enhancements on a UVLM for Nonlinear Aeroelastic Simulation. AIAA SCITECH 2022 Forum. doi:10.2514/6.2022-2455.

[25] Castrichini, A. (2017). *Parametric Assessment of a Folding Wing-Tip Device for Aircraft Loads Alleviation*. Ph.D. thesis, University of Bristol.

[26] Muñoz-Simón, A. (2021). *Vortex-lattice-based nonlinear aeroservoelastic modelling and analysis of large floating wind turbines*. Ph.D. thesis, Imperial College London. doi:10.25560/96986.

[27] Murua, J., Palacios, R., and Graham, J. M. R. (2012). Applications of the unsteady vortex-lattice method in aircraft aeroelasticity and flight dynamics. *Progress in Aerospace Sciences*, 55, 46–72. ISSN 03760421. doi:10.1016/j.paerosci.2012.06.001.

[28] Artola, M., Goizueta, N., Wynn, A., et al. (2021). Proof of Concept for a Hardware-in-the-Loop Nonlinear Control Framework for Very Flexible Aircraft. In *AIAA Scitech 2021 Forum*. Reston, Virginia: American Institute of Aeronautics and Astronautics. ISBN 978-1-62410-609-5. doi:10.2514/6.2021-1392.

[29] del Carre, A. and Palacios, R. (2020). Simulation and Optimization of Takeoff Maneuvers of Very Flexible Aircraft. *Journal of Aircraft*, 57(6), 1097–1110. ISSN 1533-3868. doi:10.2514/1.C035901.

COPYRIGHT STATEMENT